Int J Adv Manuf Technol (2018) 95:921–935
https://doi.org/10.1007/s00170-017-1238-5

ORIGINAL ARTICLE

Forming behavior and microstructural evolution during single point incremental forming process of AA-6061 aluminum alloy sheet

Vivek Kumar Barnwal[1,2,3] · **Shanta Chakrabarty**[4] · **Asim Tewari**[1,2] · **K. Narasimhan**[4] · **Sushil K. Mishra**[1]

Received: 30 July 2017 / Accepted: 24 October 2017 / Published online: 6 November 2017

Abstract AA-6061 aluminum alloy is extensively used in automobile and aerospace industries due to its high strength-to-weight ratio. However, this material shows limited formability in age-hardened condition at room temperature. Therefore, a new forming method known as single point incremental forming (SPIF) to deform the sheet was adopted. The SPIF experiments and finite element method (FEM) simulation were performed to form the sheet into the desired conical shape. Digital image correlation (DIC) method was used to measure the major and minor strains post deformation experimentally, and results were compared with FEM results. Detailed microstructural study was performed to understand the deformation behavior of AA-6061 aluminum alloy sheets during SPIF. It is observed that plastic anisotropy has strong effect on microstructure and texture development in different directions of AA-6061 alloy sheet during SPIF. It is also observed that volume fraction of goss and S texture components remains stable, whereas volume fraction of cube and brass texture changes significantly.

✉ Vivek Kumar Barnwal
vivekkumar.barnwal@gmail.com

[1] Department of Mechanical Engineering, Indian Institute of Technology Bombay, Powai, Mumbai 400076, India

[2] National Centre for Aerospace Innovation and Research, Indian Institute of Technology Bombay, Powai, Mumbai 400076, India

[3] Graduate Institute of Ferrous Technology, Pohang University of Science and Technology (POSTECH)- 77 Cheongam-ro, Nam-gu, Pohang, Gyeongbuk 37673, South Korea

[4] Department of Metallurgical Engineering and Materials Science, Indian Institute of Technology Bombay, Powai, Mumbai 400076, India

Keywords Single point incremental forming · Digital image correlation · Finite element methods · Deformation mechanism · Microstructure · Crystallographic texture

1 Introduction

AA-6061 aluminum alloy sheet is primarily an Al–Mg–Si-based precipitation hardened alloy [1]. It is commonly used in aerospace and automobile industries for structural applications due to its high strength-to-weight ratio combined with excellent corrosion resistance properties. This alloy also possesses comparatively better weldability than other heat treatable aluminum alloys [2–4]. This material is mostly used in age-hardened (T6) condition due to its high strength [5–7]. Continued design and technology improvements have further increased the demand of high-strength materials with higher formability in sheet metal alloys especially for complex shape components [8]. The maximum formability achieved in AA-6061 aluminum alloy was found in the range of 12 to 34% under different strain paths [6]. Therefore, a non-conventional sheet forming method such as incremental sheet forming (ISF) has been developed to further enhance the formability of sheet metals [9]. ISF is a highly flexible and innovative process to deform the sheet into the desired product [10]. The process completely eliminates the need for dedicated dies and also increases the sheet formability significantly. Many variations of the process are available and most important processes are single point incremental forming (SPIF) and two point incremental forming (TPIF) [11]. The SPIF process is used in the present study to deform a conical shape of AA-6061 alloy sheet.

Various studies have been performed and reported in literature to understand the deformation mechanism facilitating higher formability and effect of process parameters on the metal sheet in SPIF process [12–16]. Various factors affecting

deformation mechanisms such as through thickness shear, effect of contact stress, bending under tension (BUT), cyclic effects, and effect of hydrostatic pressure have been reported by various researchers on SPIF process [17–19]. Different deformation mechanisms are found to be applicable for different metals and final shape of the product [13, 17, 18, 20]. Jackson and Allwood (2009) studied the SPIF process for copper alloy plate and described the deformation as a combination of shear and stretching and associated the significant amount of strain to shear [18]. Presence of contact stresses has also been found to be a potential reason for enhanced formability in SPIF [17, 21]. Effect of bending under tension and cyclic loading is also suggested for the deformation mechanism in SPIF leading to higher formability [17, 19]. Pandivelan and Jeevanantham studied this process for AA-6061 alloy and found higher formability in SPIF compared to conventional forming. Effect of plastic anisotropy was also reported in this work [22]. However, all these results suggest the need for further investigation to understand the forming behavior in detail, especially for the age hardenable aluminum alloys.

The age hardenable aluminum alloys (AA-6061 alloy) exhibit complex microstructure variation during plastic deformation. Further, the plastic anisotropy behavior of the sheet leads to even more complex microstructure and crystallographic texture variation during deformation of the sheet [23]. It is well established that microstructure and crystallographic texture development play an important role in determining the plastic behavior of any sheet metal during deformation [2, 23], whereas very few microstructural and texture studies are reported to explain the deformation behavior in SPIF process. Though various works have been reported on texture evolution for AA-6061 aluminum alloy sheet, most of these works were performed for conventional forming process. Results obtained from these studies have shown that AA-6061 aluminum alloy sheet tends to show presence of beta fibers due to its FCC crystal structure. These beta fibers consist of cube, goss, brass, S, and Cu texture components [24–29]. However, no enough study has been done to examine texture development during SPIF process of AA-6061 aluminum alloy. Therefore, there is a strong need to understand the process using microstructural characterization integrated with numerical modeling to understand the forming behavior in SPIF process.

The objective of this work is to understand the macro and micro deformation behavior of SPIF process for AA-6061 aluminum alloy sheet. The SPIF process was performed on an AA-6061 aluminum alloy sheet, and deformed sheet was characterized using different techniques. Strain distribution was studied to understand the mode of the deformation during SPIF process. Thinning behavior of the sheet was also studied and compared with sin law of thinning. The finite element method (FEM) study was performed using Pamstamp-2G, and simulation results were compared with experimental results. Microstructural techniques, such as EBSD and XRD, were used to understand the effect of plastic anisotropy in the AA-6061 aluminum alloy sheet. Effect of deformation on microstructural features, such as grain size, grain shape aspect ratio, and misorientation development and crystallographic texture development of the sheet was observed and compared for different directions of the sheet.

2 Experiments

The SPIF was performed on an AA-6061 (T6) aluminum alloy sheet having a thickness of 1 mm. The chemical composition of the sheet was determined using wet chemical analysis and is given in Table 1. Mechanical properties of as received materials were calculated using uniaxial tensile tests and *r*-bar tests. Tensile tests were performed as per ASTM E8 standard on 5kN, Instron-5825 screw-driven universal testing machine [30]. An extensometer of 50 mm gauge length was used to measure the strain during deformation for accurate strain measurements. Tensile test samples were machined in three different directions from rolling direction 0° (RD), 45° (ID), and 90° (TD) as shown in Fig. 1. A minimum of three samples from each direction were tested to ensure repeatability of the results. All tensile tests were performed at room temperature and strain rate of 10^{-3} per second. The *r*-bar tests were performed to evaluate the plastic anisotropy ratio ("*r*" value) of the sheet. Test samples were prepared as per ASTM E517 standard in three different directions (RD, ID, and TD) similar to the tensile tests [31].

The SPIF process was used to achieve a conical shape from the AA-6061 (T6) aluminum alloy sheet. The SPIF process was performed on a three-axis CNC milling machine (Hardinge VMC-600 make) attached with Sinumeric-810D controller. A blank of 350 × 320 mm^2 dimension was used to form a cone having a dimension of 50-mm inner diameter and 130-mm outer diameter and 45° wall angle. The blank was clamped between two blank holders, as shown in Fig. 2a, with appropriate blank holding force to avoid any slide during deformation. The outer (350 × 320 mm^2) and inner (180 × 180 mm^2) dimensions of the blank holder, shown in Fig. 2b, are such that the equivalent forces are exerted in all the directions of the blank. To avoid bending near the blank holder's corners, a minimum distance of 25 mm was maintained between the external diameter of the cone and inner dimension of the blank holder. The complete fixture setup was rigidly mounted on a CNC bed and shown in Fig. 2a. A 13-mm-diameter smooth-end hemispherical high speed steel (HSS) tool was used to deform the blank in a three-dimensional conical shape as shown in Fig. 3a. Various studies performed on SPIF show that spindle rotation speed, under a certain range, does not influence formability and forming forces during SPIF process [9]. Moreover, studies performed at a very high spindle rotation speed show marginal increase

Table 1 Chemical composition of selected material (AA-6061 aluminum alloy)

Element	Mn	Si	Cr	Cu	Ti	Zn	Fe	Mg	Others	Al
Content (wt%)	0.11	0.53	0.1	0.17	0.032	0.084	0.31	1.06	0.012	Bal.

in formability with increase in forming tool wear. The reason for this marginal increase in formability and forming tool wear is attributed to the localized heating due to higher sliding friction at higher spindle rotation speed [16]. Therefore, the spindle rotation speed is chosen such that the sliding friction is minimized (to avoid tool wear) during SPIF [18]. Spindle rotation speed, tool linear velocity, and vertical pitch were set to 42 RPM, 10 mm per second and 0.3 mm respectively. Castor oil was used to minimize the friction between blank and forming tool. A spiral tool path was fed to the controller of the CNC to form the desired 3D shape as shown in Fig. 3b. Surface roughness on the deformed region (wall of the cone) was measured using Wyko NT8000 made white light interferometry. Digital image correlation (DIC) technique was adopted to determine the surface strains after the forming. Regular black color dots were printed on one side of the blank prior to deformation using screen printing technique, shown in Fig. 3c, and opposite surface was used for SPIF process [32]. A series of images was captured from different orientations before and after the SPIF deformation. These images were analyzed in "ARGUS" DIC software to analyze the strain distribution across the blank.

Microstructural analysis of the deformed blank was performed using electron backscattering diffraction (EBSD) technique. Different samples, UD (undeform), RD (along rolling direction), ID (45° to rolling direction), and TD (90° to rolling direction), were selected from deformed specimen for detailed microstructural analysis as shown in Fig. 4.

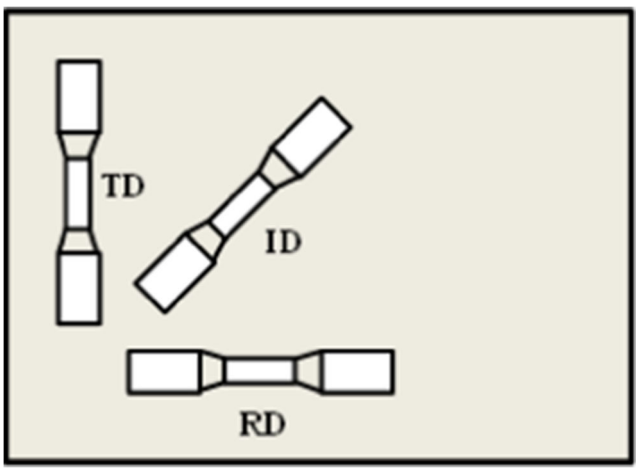

Fig. 1 Schematic diagram for tensile sample preparation in three different directions (RD, ID, TD) of the AA-6061 aluminum alloy sheet

The sample surface was prepared for EBSD analysis by polishing with progressively finer water-based diamond suspensions (to a size of 1 μm). Finally, electro-polishing was carried out using A2 electrolyte (STRUERS®) at 13 V for 16 s. EBSD scans with 0.3 μm step size were carried out using a FEI Quanta™ 200 Hv scanning electron microscope equipped with TSL OIM™ orientation imaging microscopy software. EBSD data were utilized to estimate the misorientation development, Taylor factor, and grain shape. These same samples were used for bulk texture analysis using "Panalytical MRD" X-ray system. X-ray ODFs and texture index (TI) were estimated for each sample by the inversion of three to four incomplete pole figures of corresponding phases using the MTM-FHM (K. U. Leuven, Department MTM-fast harmonic measurements) program [33].

3 Simulations

FEM study of SPIF process was performed using material properties as given in Table 2. A commercial FEM-based program, PAMSTAMP 2G, was used to simulate the SPIF experimental process. Three-dimensional surface models of all the tools used in SPIF process such as blank holders, hemispherical tool, and blank were created using SolidWorks and are shown in Fig. 5a. Geometries and dimensions of all the tools and blank were kept similar to the experimental setup. Appropriate boundary conditions similar to experiments were applied to perform the SPIF simulation and shown in Fig. 5b.

Blank holders were considered as rigid bodies, and their movements were fixed in all the directions (i.e., rotation and translation in x-y-z direction). Similarly, the hemispherical tool was also assumed as a rigid body and only rotational movement was applied to it in z-direction. The tool movements about x, y, and z axes were given similar to experimental SPIF spiral tool path as given in Fig. 3b. Four-node shell elements were used for discretization of the blank with an element size of 1 mm. Hill-48 criterion and direct experimental true stress-true strain data were used to describe yielding and hardening behavior of the material respectively. Different "r" values (as per Table 2) for different directions of the blank (RD, ID, and TD) were used to analyze the effect of plastic anisotropy. A total of 16 nodes (exactly at location of bolts used for clamping in SPIF experiment) were selected and fixed in all the directions and shown in Fig. 5b. The coulomb friction between the blank and hemispherical tool was

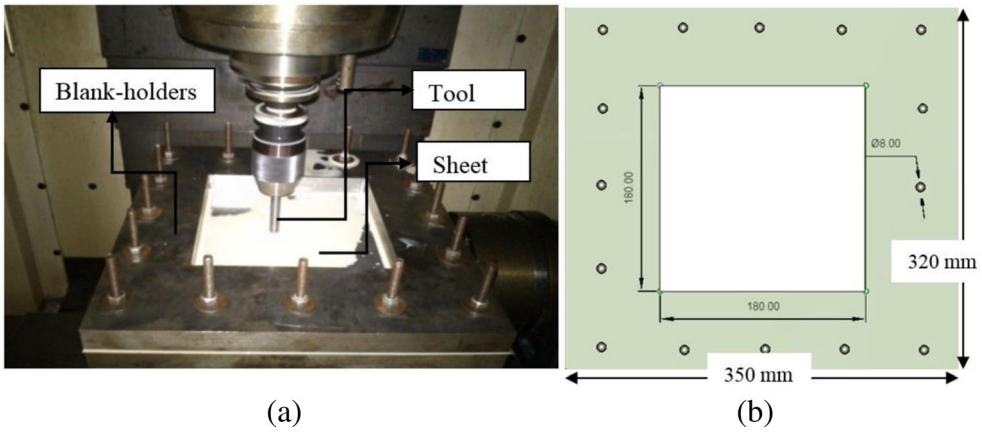

Fig. 2 **a** Experimental setup used for SPIF process and **b** detailed geometry and dimensions of blank holders used in SPIF process

assumed to be 0.08 [34]. Similarly, the friction between blank holders and blank was assumed to be 0.12 [34].

4 Result and discussion

Tensile tests and *r*-bar tests were performed to obtain mechanical properties of the sheet in three different directions (RD, ID, and TD), and the results are tabulated in Table 2. The results show that proof stress (PS) and tensile strength (TS) of the sheet are almost similar in RD and ID directions, whereas slightly lower values of PS and TS were achieved in TD direction. The strain hardening exponent (n) and strength factor (K) values (calculated using the Hollomon law) were approximately equal in RD, ID, and TD directions. However, this material shows major difference in "r" values at different directions. The minimum and maximum "r" values of this sheet are 0.558 and 0.833 in RD and TD directions respectively. The ID direction of the sheet possesses an intermediate "r" value of 0.704. Based on "r" values at different directions, the normal anisotropy of the sheet was calculated to be 0.7.

The AA-6061 aluminum alloy sheet was subjected to SPIF process to form a conical shape of 130-mm outer diameter, 50-mm inner diameter, and 45° wall angle. The hemispherical tool's dimension and vertical pitch for SPIF process were selected based on previous studies performed on aluminum alloys such that minimum surface roughness is achieved on the deformed surface after SPIF process [35, 36]. The ratio of the tool diameter (13 mm) and vertical pitch (0.3 mm) values were kept close to 40 to achieve minimum surface roughness (R_a value) [36, 37]. The tool rotation speed (RPM) was calculated based on Eq. 1 such that the sliding friction during SPIF

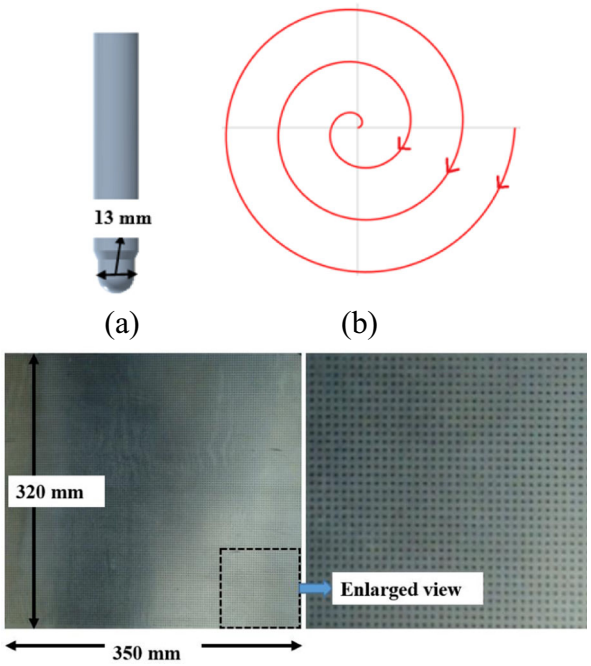

Fig. 3 Basic elements used in SPIF process: **a** hemispherical forming tool, **b** circular spiral tool path, and **c** AA-6061 alloy blank with circular grid pattern (c) Distance between two circle is 2.5 mm and the diameter of each circle is 1.0 mm

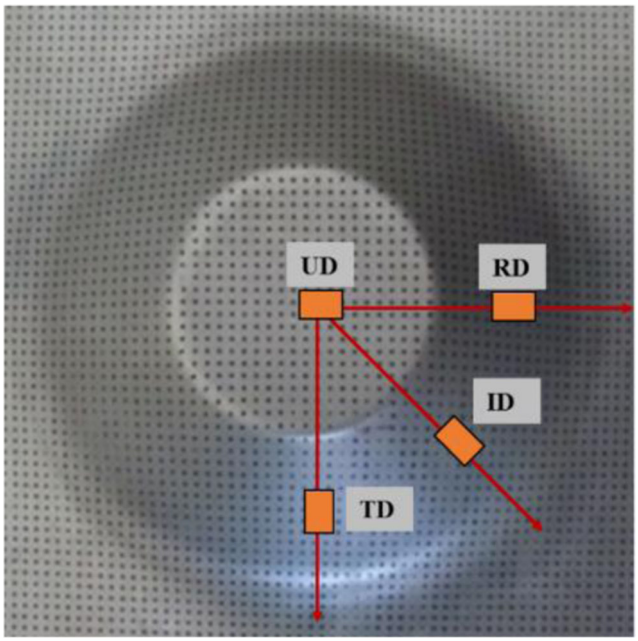

Fig. 4 Various regions (undeformed, RD, ID, and TD) selected for microstructural characterization and analysis on deformed SPIF cone

process remains minimum [18]. The SPIF process was performed with 42 RPM of spindle rotation speed and 10 mm/s of tool linear velocity.

$$\omega = v/\left(\pi.r\sqrt{1/2(1-\cos 2\varphi)}\right) \quad (1)$$

where, ω = spindle rotation speed, υ = linear tool speed, r = tool radius, and φ = wall angle.

A conical shape was successfully formed using the SPIF process, and top and bottom surfaces after the deformation are given in Fig. 6a, b respectively. The surface roughness was measured on the deformed region where the forming tool was directly in contact with the blank (bottom surface). The average R_a value (1.28 ± 0.37 μm) at the deformed region was very close to the study performed by Durante et al. on aluminum alloys [35] and no wrinkling was observed on the deformed blank. The deformed blank was divided into three different regions (Fig. 6): blank (B), deformed (D), and undeformed region (U). The D region underwent maximum interactions between forming tool and blank, whereas the U region did not have any interaction between tool and blank. The B and U regions are the regions where no deformation was intended; however, marginal bending was observed.

The strain distribution on the deformed blank was measured using the DIC technique. The major, minor, and thickness true strain distributions on the deformed surface are shown in Fig. 7a, c respectively. The thickness strain was calculated based on the volume constancy law ($\varepsilon_1 + \varepsilon_2 + \varepsilon_3 = 0$) during plastic deformation [38]. Major and minor true strains during deformation of the sheet were plotted against the section length of the blank and shown in Fig. 8. Approximately constant major and minor true strain values were obtained throughout the wall (D region) of the cone as shown in Fig. 8.

Values of major true strain were found to be in the range of 0.30 to 0.35 in the deformed region of the SPIF cone, whereas relatively very small or negligible minor true strain values were obtained in the same region (deformed region) of the blank. This indicates that the deformation on the SPIF cone's wall undergoes plane strain deformation similar to other studies [18, 39]. It has also been found that the direction of major true strain is always perpendicular to the tool path as shown in Fig. 9. This observation is experimental evidence of the major true strain direction during SPIF process reported in the literature [18]. This can be attributed to the flow of the material in the sheet to the normal direction of tool direction. Similarly, thickness of the blank was evaluated against the section length of the sheet and shown in Fig. 10. It can be observed that sheet thickness also remains almost constant throughout the deformed region of the blank and no strain localization was observed. The thickness distribution in the deformed region was compared with sin law of thinning as given in Eq. 2 [18]. The thickness true strain at the deformed region follows the sin law of thinning as shown in Fig. 10. The blank thickness in deformed region of the sheet was found to be approximately 0.7 mm.

$$t_f = t_0{}^{*}\sin\left(\prod/2-\varphi\right) \quad (2)$$

where t_f = final thickness, t_0 = initial thickness, and φ = wall angle

The conical shape was also achieved by FEM simulation using material properties and SPIF parameters as in experiments. Figure 11a, b shows the top and bottom (blank and tool contact) surfaces, respectively, of the deformed AA-6061

Table 2 Mechanical properties of AA-6061 (T6) aluminum alloy obtained using tensile tests and *r*-bar tests

	PS (MPa)	UTS (MPa)	Elongation (%)	*K*	*n*	Plastic anisotropy	$\bar{r}_{mean}$
RD	265	308	14.45	416	0.10	$r_0 = 0.558$	0.70
ID	255	293	12.36	415	0.10	$r_{45} = 0.70$	
TD	238	274	13.06	406	0.09	$r_{90} = 0.833$	

PS proof stress, *UTS* ultimate tensile strength, *K* strength coefficient, *n* strain hardening exponent

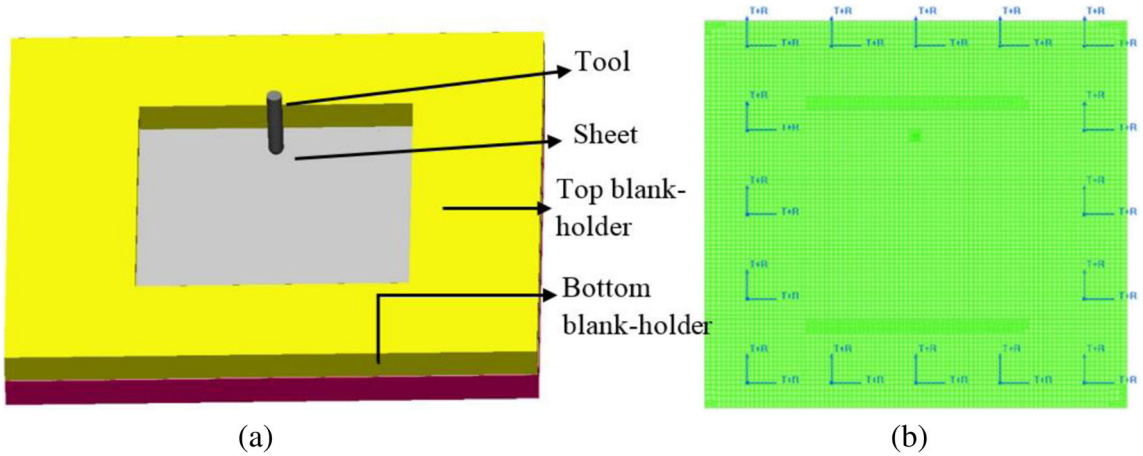

Fig. 5 **a** Arrangement of various forming tools in SPIF simulation and **b** boundary conditions (locations of the nodes to be fixed) in SPIF simulation

alloy sheet obtained from SPIF simulations. The simulated deformed surface clearly shows unevenness when compared to the experimental deformed surface.

The major, minor, and thickness true strain distribution across the blank after deformation is shown in Fig. 12a–c respectively. Similar to the experimental results, higher major true strain values were obtained in the deformed region of the blank compared to the two other regions (blank and undeformed) as shown in Fig. 12a. Similar behavior can be observed for the thickness distribution of the blank Fig. 12c. The minor true strain values remain relatively small compared to the major true strain values in the deformed region of the sheet (Fig. 12b). The direction of major true strain and tool path is shown in Fig. 12d with corresponding notation shown in Fig. 12e.

The direction of the major true strain is always found to be perpendicular to the tool travel direction similar to the experimental observation. The major and minor true strain values for experiment and simulation are plotted together for comparison and shown in Fig. 13. Experimental and simulation strains are represented by regular lines and dotted lines respectively. Though the average strain developed in the deformed regions is almost same for experiment and simulation, the variation in strain along the deformed regions is very large in simulation.

This variation in strain can be clearly observed in the deformed sample as uneven surface (Fig. 11). The variation can be attributed to the coarse mesh size of the element in simulation, considering the nature of the SPIF process. The contact area (between blank and tool) in this process is very small and localized which requires a very fine mesh size. By lowering the mesh size, the variation in strain decreased and smooth surfaces were observed but simulation could not be completed successfully due to limitation in computational capabilities. Therefore, a relatively coarse mesh size of 1 mm was used to complete the SPIF simulation successfully. Figure 14 compares the thickness distribution obtained from simulation and experiment. Here again, the average thickness strain distribution is found to be in good agreement with the experimental results with large variation in strains in simulation.

As shown in Table 2, "*r*" values of the sheet vary in three different directions (RD, ID, and TD), which may affect the deformation behavior at these directions of the sheet. To study this, a total of five points along each direction were considered

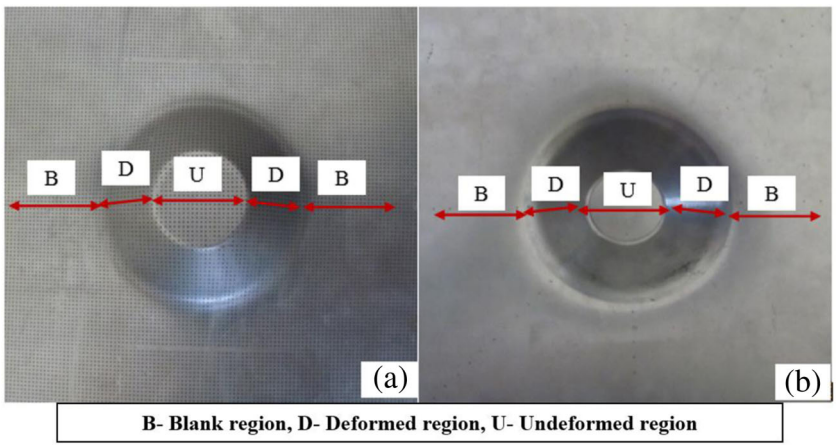

Fig. 6 Various regions on AA-6061 alloy cone deformed using SPIF experiment at **a** top surface and **b** bottom (work) surface of the blank

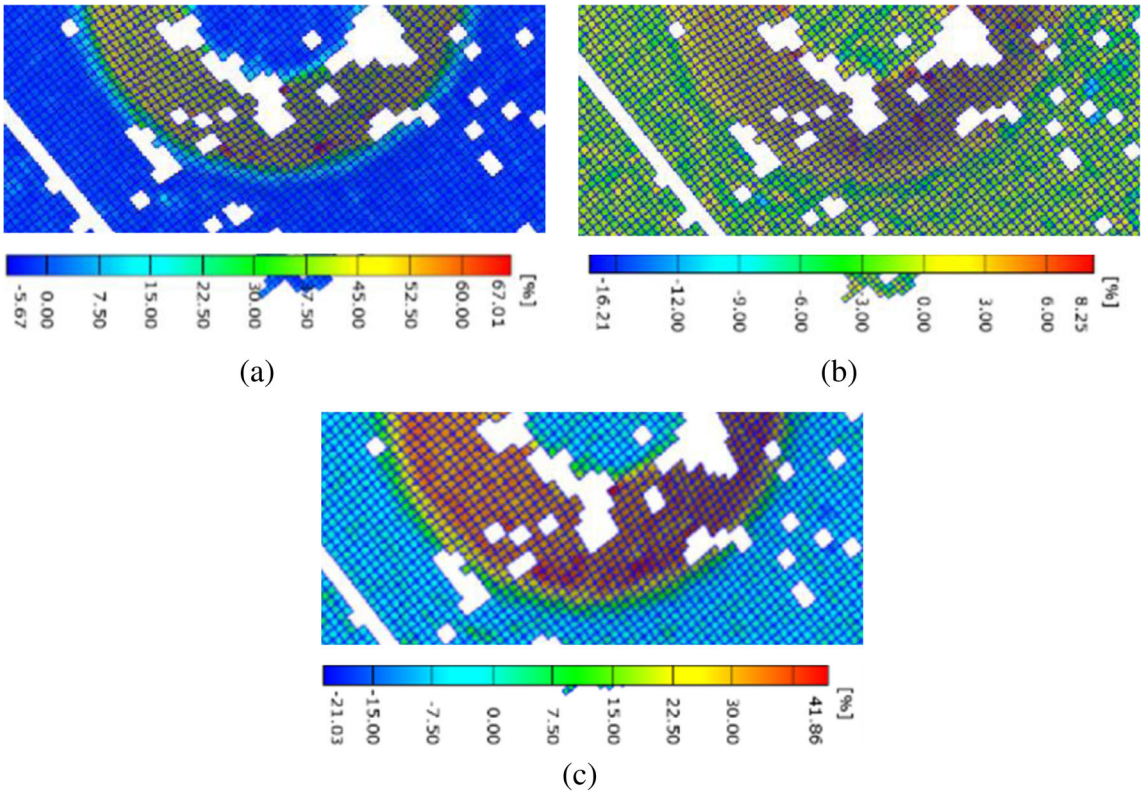

Fig. 7 Strain distribution in experimental SPIF cone. **a** Major strain. **b** Minor strain. **c** Thinning (obtained using DIC technique)

and these points were positioned at equal distance starting from the inner diameter towards the outer diameter of the cone as shown in Fig. 15.

A graph between minor and major true strains at these points on the sheet from initial deformation to final deformation was plotted and called strain path curve (SPC). The SPCs at different points for RD, ID, and TD directions are shown in Fig. 16a–c respectively. Points 1 and 5 which are at the boundary of the deformation region show minimum strain values after completion of the process, whereas points 2, 3, and 4 show significant amount of major and minor true strain values though minor true strain remains very small during the process. The SPCs are also found to be of zigzag nature which could be the possible reason for higher formability achieved in SPIF process compared to conventional forming processes [17, 40]. These behaviors are found to be consistent for all three directions (RD, ID, and TD) of the sheet. However, no clear effect of plastic anisotropy on strain distribution and strain path development was observed by simulation as strain paths remain similar for all three directions (RD, ID, and TD) during deformation.

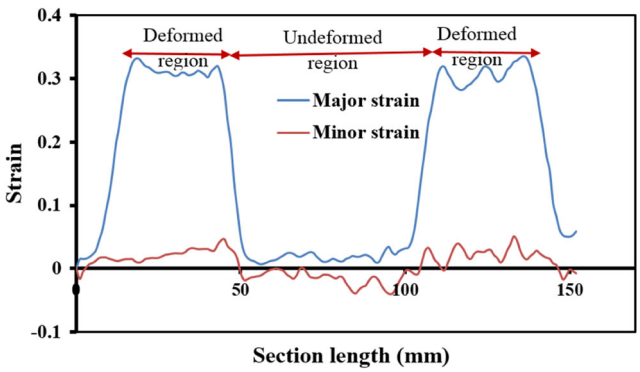

Fig. 8 Major and minor strain distributions on experimentally obtained SPIF cone (obtained using DIC technique)

In the above sections, the experimental and simulation results show that the strain distribution on the sheet surface and strain path at all three directions (RD, ID, and TD) are almost similar even though plastic anisotropy ratio ("*r*" value) varies for different sheet directions (RD, ID, and TD). Nevertheless, the deformation behavior of the sheet at different directions can be elaborated by a detailed study of microstructure and texture development during deformation. The samples were prepared for microstructural study from the deformed region of the sheet (R3, I3, and T3 as shown in Fig. 4) at all three directions and compared with the undeformed region. The microstructural studies were performed using the EBSD technique, and the same area was also used for bulk texture measurements. The inverse pole figure (IPF) maps of deformed and undeformed regions are shown in Fig. 17a–d. The color in the figure represents the crystallographic orientation in inverse pole figure notation as given in Fig. 17. The black region represents the unindexed points during EBSD scan. It can be observed from Fig. 17 that the black regions are very few in

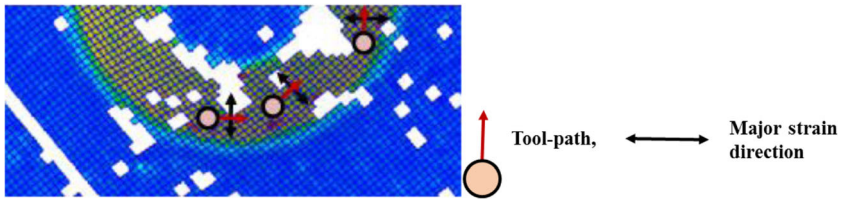

Fig. 9 Major true strain direction on experimentally obtained SPIF cone

undeformed samples (Fig. 17a) compared to deformed samples (Fig. 17b–d). The increase in unindexed points in deformed samples is due to the local strain localization or dislocation accumulations where EBSD pattern quality is very poor leading to unindexed points.

The AA-6061 alloy primarily deforms by slip mechanism which results in misorientation development and strain localization during deformation. The EBSD data can further be processed to statistically determine grain average misorientation (GAM), grain shape aspect ratio, and Taylor factor (TF) using the OIM software. Though the strain level is almost similar for all three directions (RD, ID, and TD) of the sheet, the ID sample shows a fewer number of unindexed points as compared to the other two directions. The misorientation development was measured in terms of GAM value for all the samples and plotted in Fig. 18a. The GAM quantifies the average misorientation between neighboring points within a grain [2]. The undeformed sample shows very low GAM value which may be attributed to the processing of the as received sheet and measurement uncertainty. After deformation, the GAM value increases for all three (RD, ID, and TD) directions. The samples deformed at RD and TD directions show higher misorientation development compared to those at ID direction where unindexed points are fewer. In turn, it can be understood that the slip deformation or dislocation movement in ID direction is lower as compared to that in the other two directions which could be the reason for lower ductility in ID direction (Table 2). The difference in slip activity in different directions is due to the crystallographic orientations and texture development during deformation of the sheet. TF was calculated based on EBSD data and plotted in Fig. 18b which is a scalar representation of orientation hardness. The TF can be generalized as σ/τ where σ and τ are the stress tensor and the critical resolved shear stress respectively [41]. It can be clearly seen that the TF for the ID direction is higher than for the other two directions (RD and TD). Due to high TF in the ID direction, dislocation movement is low leading to difficulty in sample deformation [41]. This may be the reason for low misorientation development in the ID sample.

Various literatures show that the plastic deformation in sheet metal may cause the grains to elongate to some degree [42]. The grain elongation is measured in terms of grain shape aspect ratio (A_r), and its value is inversely proportional to the extent of grain elongation [41]. Figure 18c shows grain shape aspect ratio in undeformed and deformed conditions for all three directions (RD, ID, and TD) of the sheet. It can be observed from this figure that the grains are more elongated in deformed condition compared to the undeformed condition. Moreover, their extent of elongation is different for all three sheet directions in the deformed condition. It can be observed that the grains in the sample prepared from ID direction are least elongated than in the sample prepared from RD and TD

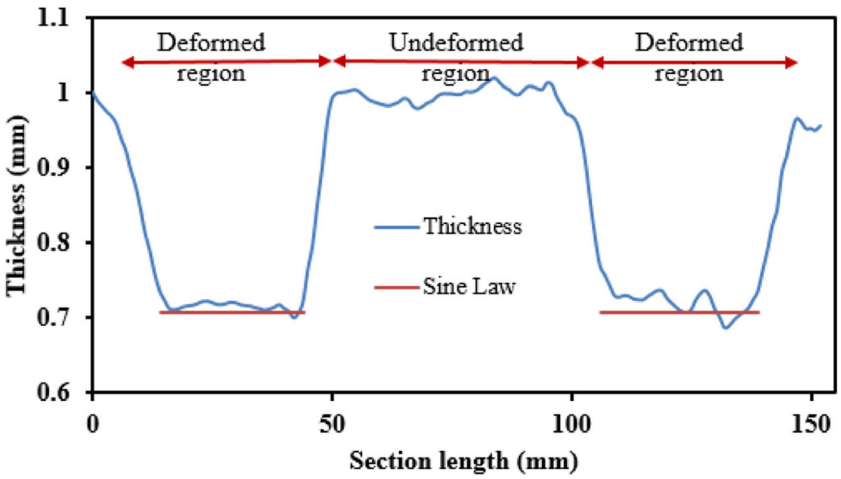

Fig. 10 Thickness distribution on experimentally obtained SPIF cone (obtained using DIC technique)

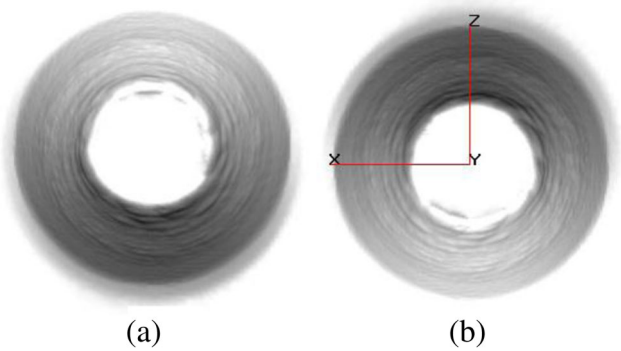

Fig. 11 Deformed surface of SPIF cone obtained from FEM simulation. **a** Top surface and **b** bottom surface

directions. This observation can be attributed to the higher Taylor's factor in the ID direction.

Aluminum alloys also develop deformed microtexture during plastic deformation of the sheet [27, 43]. Development of these crystallographic textures during deformation is a function of crystal structure, initial texture of the sheet, deformation mode, strain level, and loading condition (in turn plastic anisotropy of the sheet) [42]. The deformation behavior of the material changes as deformation texture evolves. To analyze various texture developments in samples before and after deformation at different directions (RD, ID, and TD), detailed bulk texture measurement of Al-6061 was carried out using X-ray diffraction technique. The orientation distribution function (ODF) was measured for all the samples using bulk texture measurement, where ODF is a probability density function which is used to quantify the volume fraction (frequency) of crystallographic orientations [2]. Three standard 2D ODF sections of $\Phi 2$ = 45°, 65°, and 90° are considered adequate to represent the presence of various standard texture components in an FCC sheet material [27]. From these standard ODF sections, the different texture components are identified before and after deformation, shown in Fig. 19. The maximum ODF values for corresponding undeformed and deformed specimens at different directions are given in Fig. 19. The location of standard texture components in 2D ODF sections are indicated by various symbols with different colors. The analysis of the ODF sections shows the significant presence of S {123} <634>, cube {001} <100>, copper {112} <111>, and goss {011} <100> texture components in the undeformed specimen. After deformation, these texture components vary to different extents at different directions (RD, ID, and TD). The copper {112} <111> texture present in the undeformed specimen diminishes in RD direction and disappears in other cases after deformation. The brass {011} <211> texture

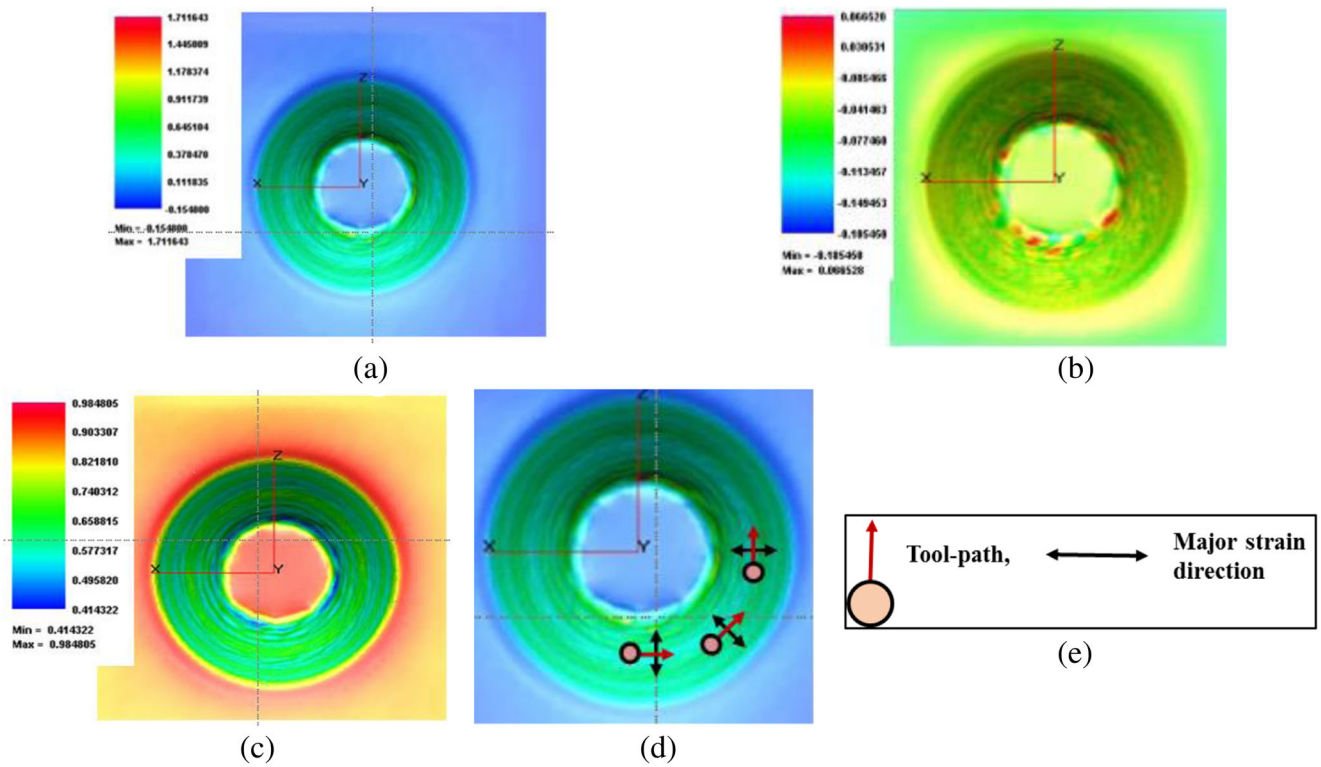

Fig. 12 Strain distribution on SPIF cone. **a** Major true strain, **b** minor true strain, **c** thickness and **d** major true strain direction obtained using FEM simulation **e** notations

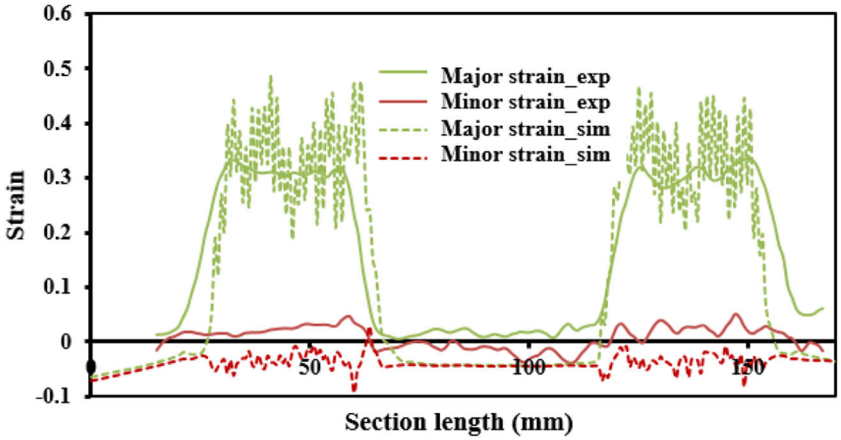

Fig. 13 Comparison of experimental and simulation results for major and minor strain distribution on deformed SPIF cone

component intensifies after deformation irrespective of directions.

To quantitatively analyze the variation of texture components in different directions, volume fraction of all the significant texture components are calculated at different directions (RD, ID, and TD) after deformation and shown in Fig. 20. The AA-6061 sheet in undeformed condition shows significantly higher volume fraction of cube {001} <100> (3.31%) and S {123} <634> (6.52%) textures and comparatively lesser amount of brass {011} <211> (1.89) and goss {011} <100> (2.36) texture components. After deformation, the volume fraction of brass {011} <211> texture increases sharply (approximately to 7.0%) in all the directions (i.e., RD, ID, and TD), whereas the volume fraction of cube {001} <100> texture reduces significantly especially in ID direction (0.6%). However, goss {011} <100> and S {123} <634> texture components remain stable and their volume fraction changes marginally in TD direction as shown in Fig. 20. From the literature, it is found that the cube-oriented grains possess higher values of Schmid factor; consequently, rotation takes place very easily during deformation as the {001} plane of cube grains rotates to {011} plane of goss orientation [44]. With increase in strain, part of the goss texture components transform to brass texture components. This might be the reason for increase in the volume fraction of brass components after deformation irrespective of direction.

It is also found from the literature that the goss ({011} <100>), brass ({011} <211>), cube ({001} <100>), and copper {112} <111> orientations influence the "*r*" value significantly [43, 44]. During deformation of aluminum alloys, the gradient of goss texture components through thickness is typically very strong as compared to other texture components. The fraction of goss orientation in mid thickness is almost three times higher than that of the surface [44]. The different through-thickness texture evolution causes the variations of the *r* value profile and influences the average *r* value [45]. The yield locus of texture component in different direction

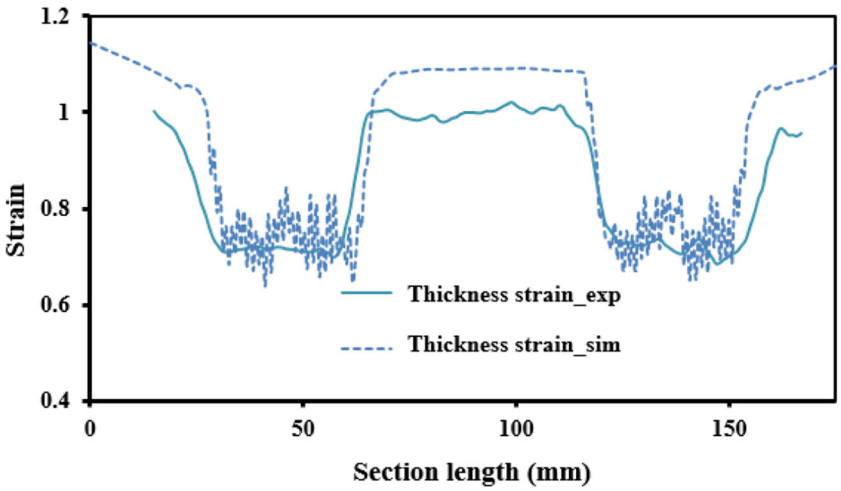

Fig. 14 Comparison of experimental and simulation results for thickness strain distribution on deformed SPIF cone

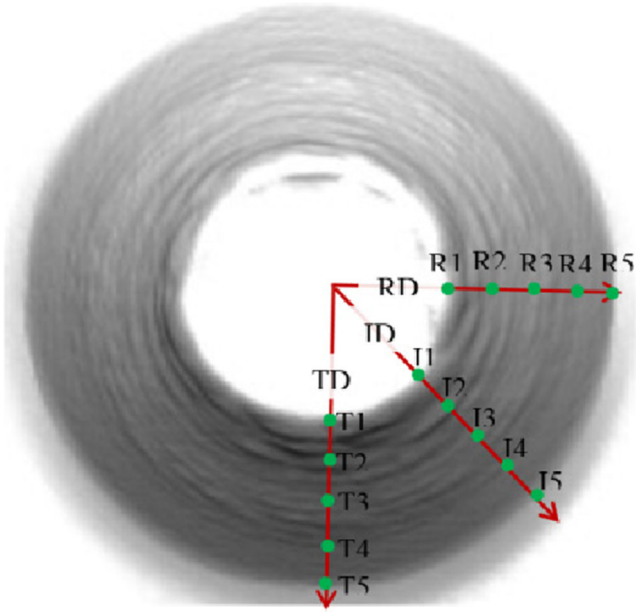

Fig. 15 Selection of multiple points at equal distance for strain path study on simulated SPIF cone surface

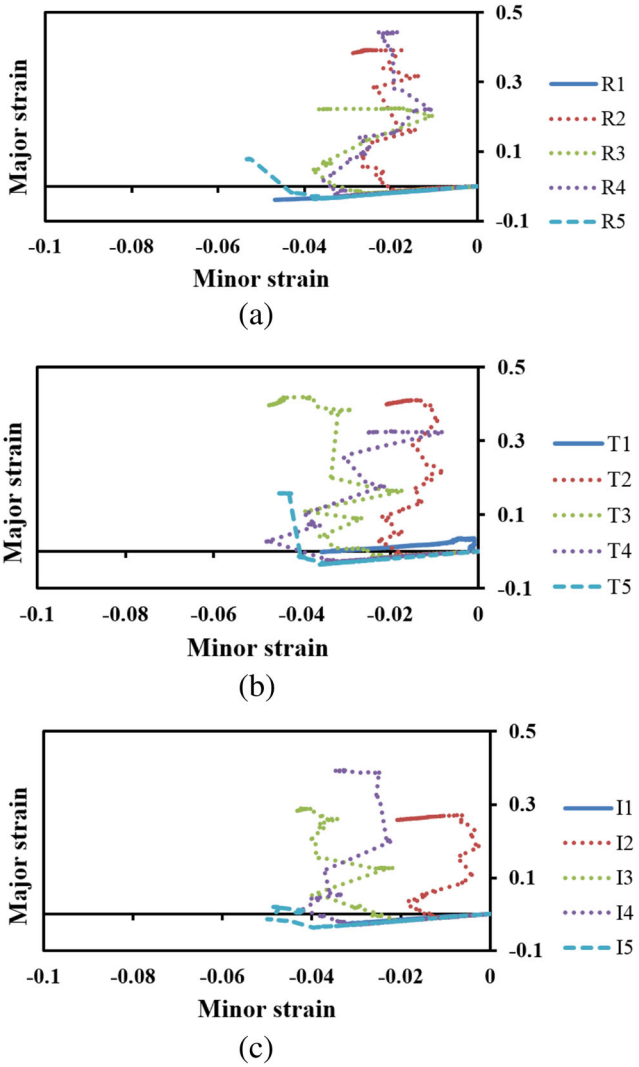

Fig. 16 Strain path study at multiple points selected along **a** RD, **b** TD, and **c** ID directions

determines the *r* value of the materials. It has been reported in the literature that the cube {001} <100> texture shows yield locus as per the von Mises criterion in the RD and TD directions, whereas in the ID direction, the yield locus become circular. It corresponds to a lower *r* value at ID and higher at RD and TD direction. Similarly, the brass {011} <211>, S {123} <634>, and copper {112} <111> types of texture show slender yield loci in the ID directions and short and thick yield loci in the RD and TD directions. Hence, these texture components give a higher *r* value in the ID directions and a lower *r* value in the RD and TD directions. In the present study (Figs. 19 and 20), though the cube {001} <100> texture component decreases with deformation, however, the fraction present in TD and RD directions is almost equal and less in ID direction. Similarly, the fraction of S {123} <634> texture components is less in ID direction and equal in both TD and RD directions. The fraction of brass {011} <211> component is more in TD direction, whereas the copper {112} <111> texture is only present in RD direction and absent in both ID and TD directions. Based on the directional behavior of yield locus of texture components, the presence of higher fraction of cube {001} <100> component in TD direction enhances the *r* value in TD than in ID direction and the presence of copper {112} <111> texture component in only RD direction might be the reason behind the observation of lowest "*r*" value in RD direction in the present material compared to ID and TD directions.

The texturing of the material and relative anisotropy can be quantitatively described by two parameters: TI and maximum orientation distribution function (ODF) intensity. TI can be represented by Eq. 3 where $f(g)$ is the ODF intensity and can be used to represent the relative texturing or anisotropy [2].

$$TI = \int f(g)^2 dg \tag{3}$$

TI from bulk texture analyses of undeformed and deformed specimens at different directions were estimated and are shown in Fig. 21.

It can be clearly observed from this figure that the sheet has comparatively higher TI value in the deformed condition (1.79–1.94) than in the undeformed condition (1.48). Furthermore, this deformed blank shows lowest TI value in ID direction (1.788) and highest TI value in RD direction (1.94). This is due to the fact that the Taylor factor value was highest for ID and lowest for RD directions. Therefore, ID direction experiences least dislocation accumulation, whereas RD direction experiences highest dislocation accumulation during SPIF process of this alloy. Due to

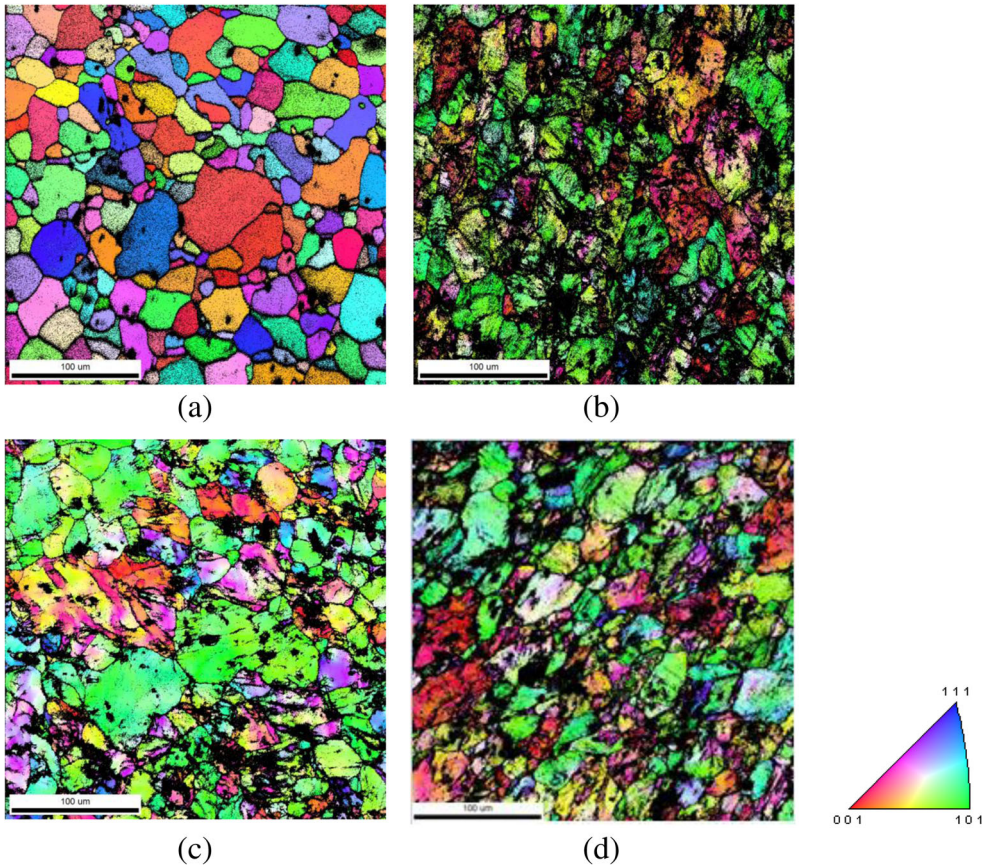

Fig. 17 Inverse pole figure (IPF) maps of specimens at different conditions and directions. **a** Undeformed, **b** RD (deformed), **c** ID (deformed), and **d** TD (deformed) to study the effect of SPIF deformation on microstructure evolution

development of deformation texture, deformation behavior changes for different directions (RD, ID, and TD) of the sheets. Though plastic anisotropy of this sheet is intermediate in ID direction, the Taylor factor increases due to deformation texture development, leading to less slip activity in ID direction.

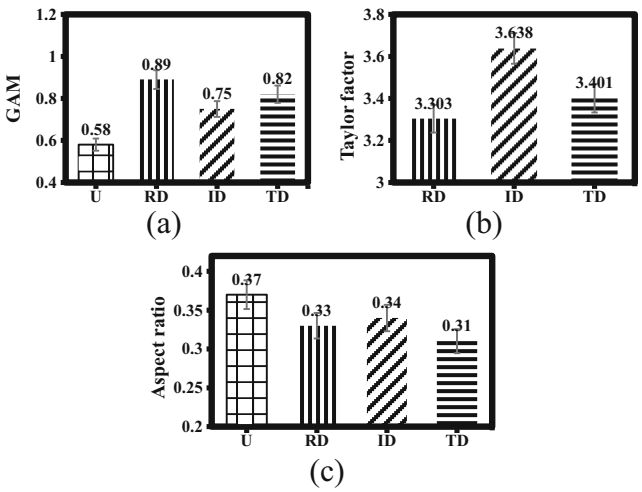

Fig. 18 Effect of SPIF deformation on various microstructural features such as **a** grain average misorientation (GAM), **b** Taylor factor, and **c** grain shape aspect ratio in undeformed and deformed (RD, ID, and TD directions) conditions

5 Summary and conclusions

The SPIF process was performed on a AA-6061 aluminum sheet alloy using appropriate process parameters, and a conical shape was achieved. The surface strains were measured using a DIC technique on the sheet. The FEM study was also performed for same metal and SPIF process using appropriate material models and process parameters, and the results were compared with experimental results. To achieve microstructural properties, samples were prepared from undeformed and deformed regions of the sheet. The effect of plastic anisotropy on AA-6061 aluminum alloy sheet in SPIF process was observed using EBSD and XRD techniques. Various conclusions drawn from this study are as below:

1. The results obtained from SPIF experiments and simulations show very clearly that metal sheet undergoes plane strain mode of deformation during SPIF process. It is also found that the direction of major principal strain is always perpendicular to tool travel direction. This implies that flow of metal in SPIF process is also always perpendicular to the tool travel direction.
2. FEM study shows that simulation results are in good agreement with experimental results. However, more

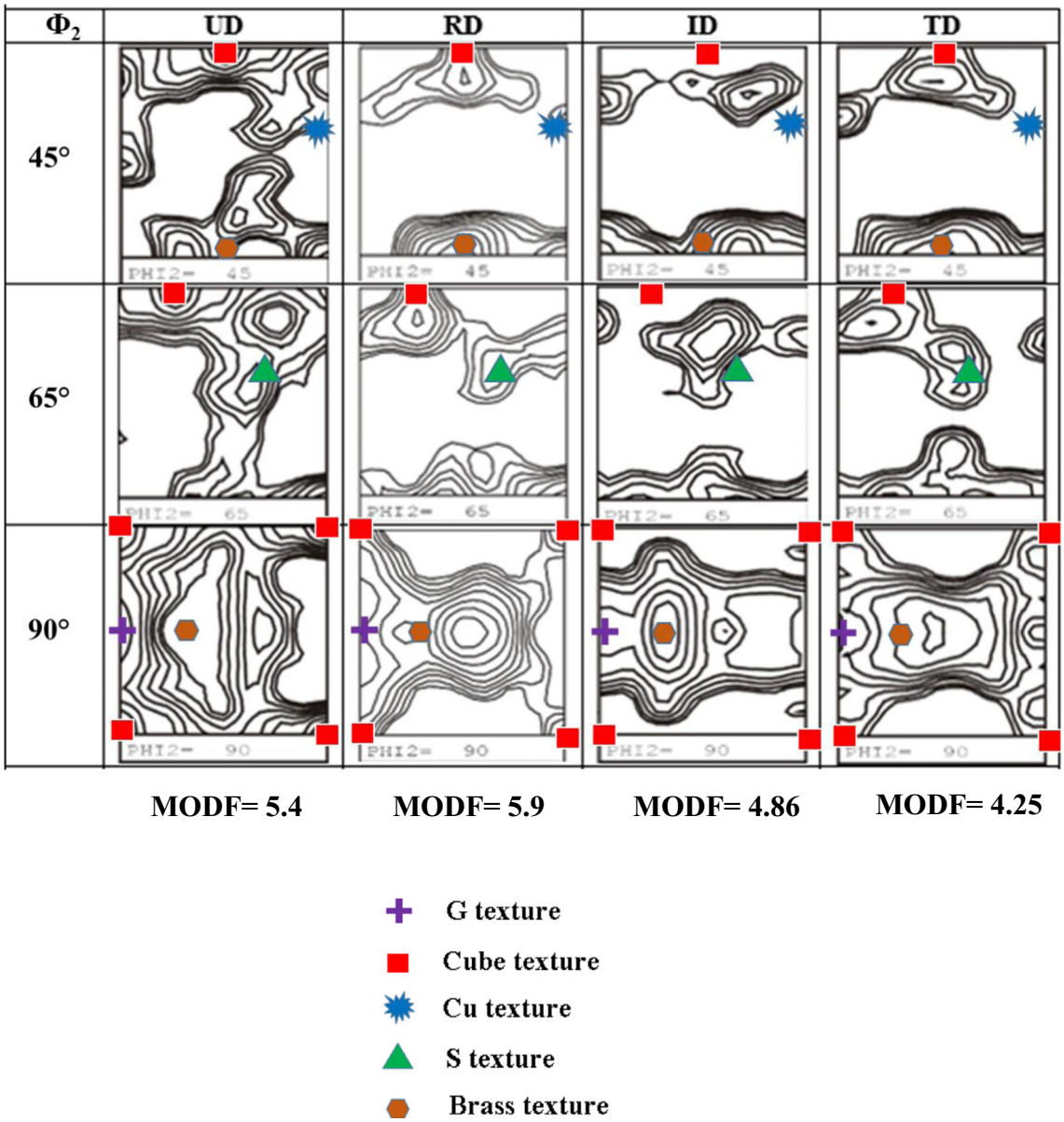

Fig. 19 Effect of SPIF deformation on texture evolution shown by using orientation distribution function (ODF) in undeformed and deformed (RD, ID, and TD directions) conditions

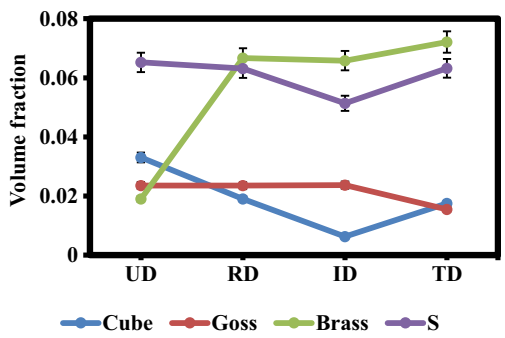

Fig. 20 Effect of SPIF deformation on volume fractions of different texture components at undeformed and deformed conditions (for RD, ID, and TD directions)

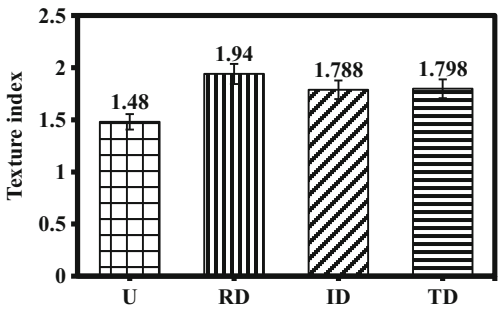

Fig. 21 Effect of SPIF deformation on texture evolution in terms of TI at undeformed and deformed conditions (for RD, ID, and TD directions)

accurate results can be achieved by using very fine mesh size as deformation is very localized at any given instant in SPIF process.

3. The detailed microstructural study shows that this metal offers highest resistance to deformation in ID direction during SPIF process leading to least misorientation development (GAM), grain elongation, and texture development (TI). The main reason for higher resistance to deformation in ID direction is a higher Taylor factor (TF) in ID direction compared to RD and TD directions.
4. Bulk texture analysis shows that volume fraction of goss and S texture components remains stable, whereas volume fraction of cube and brass texture changes significantly. This can be attributed to the possible rotation of cube texture to brass texture through goss texture at high strain level.

Acknowledgements The authors gratefully acknowledge the financial support provided for this work by the National Centre for Aerospace Innovation and Research, IIT Bombay, Powai, Mumbai, India.

References

1. Raghavan RS, Tiwari SM, Mishra SK, Carsley JE (2014) Recovery quantification and onset of recrystallization in aluminium alloys. Philos Mag Lett 94:755–763
2. Davies ER (2008) Introduction to texture analysis. Handbook of Texture Analysis Imperial College Press
3. Mahabunphachai S, Koç M (2010) Investigations on forming of aluminum 5052 and 6061 sheet alloys at warm temperatures. Mater Des 31:2422–2434
4. Demir H, Gündüz S (2009) The effects of aging on machinability of 6061 aluminium alloy. Mater Des 30:1480–1483
5. Raju P, Venkateswarlu G, Davidson MJ (2012) Formability studies on AA 6061 sheet metal for automotive body structures using deform-2D. Int J Adv Sci Tech Res 4:638–644
6. Barnwal VK, Tewari A, Narasimhan K, Mishra SK (2016) Effect of plastic anisotropy on forming behavior of AA-6061 aluminum alloy sheet. J Strain Anal Eng Des 51:507–517
7. Mariani E, Ghassemieh E (2010) Microstructure evolution of 6061 O Al alloy during ultrasonic consolidation: an insight from electron backscatter diffraction. Acta Mater 58:2492–2503
8. Wong CC, Ta D, Lin J (2003) A review of spinning, shear forming and flow forming processes. Int J Mach Tools Manuf 43:1419–1435
9. Buffa G, Campanella D, Fratini L (2012) On the improvement of material formability in SPIF operation through tool stirring action. Int J Adv Manuf Technol 66:1343–1351
10. Aerens R, Eyckens P, Bael A, Duflou JR (2009) Force prediction for single point incremental forming deduced from experimental and FEM observations. Int J Adv Manuf Technol 46:969–982
11. Jeswiet J, Duflou JR, Szekeres A (2005) Forces in single point and two point incremental forming. Adv Mater Res 6–8:449–456
12. Park JJ, Kim YH (2003) Fundamental studies on the incremental sheet metal forming technique. J Mater Process Technol 140:447–453
13. Malhotra R, Xue L, Belytschko T, Cao J (2012) Mechanics of fracture in single point incremental forming. J Mater Process Technol 212:1573–1590
14. Eyckens P, Belkassem B, Henrard C, Gu J, Sol H, Habraken AM, Duflou JR, Bael A, Houtte P (2010) Strain evolution in the single point incremental forming process: digital image correlation measurement and finite element prediction. Int J Mater Form 4:55–71
15. Silva MB, Nielsen PS, Bay N, Martins PF (2011) Failure mechanisms in single-point incremental forming of metals. Int J Adv Manuf Technol 56:893–903
16. Ambrogio G, Filice L, Gagliardi F (2011) Enhancing incremental sheet forming performance using high speed. Key Eng Mater 473:847–852
17. Emmens WC, van den Boogaard AH (2009) An overview of stabilizing deformation mechanisms in incremental sheet forming. J Mater Process Technol 209:3688–3695
18. Jackson K, Allwood J (2009) The mechanics of incremental sheet forming. J Mater Process Technol 209:1158–1174
19. Emmens WC, van den Boogaard AH (2009) Incremental forming by continuous bending under tension—an experimental investigation. J Mater Process Technol 209:5456–5463
20. Fiorentino a (2013) Force-based failure criterion in incremental sheet forming. Int J Adv Manuf Technol 68:557–563
21. Bambach S, Hirt MG (2003) Modelling and experimental evaluation of the incremental CNC sheet metal forming process. In: Proceedings 7th COMPLAS
22. Pandivelan C, Jeevanantham AK (2015) Formability evaluation of AA 6061 alloy sheets on single point incremental forming using CNC vertical milling Machin. J Mater Environ Sci 6:1343–1353
23. Barnwal VK, Raghavan R, Tewari A, Narasimhan K, Mishra SK (2017) Effect of microstructure and texture on forming behaviour of AA-6061 aluminium alloy sheet. Mater Sci Eng A 679:56–65
24. Mishin OV, Bay B, Jensen DJ (2000) Through-thickness texture gradients in cold-rolled aluminum. Metall Mater Trans A 31:1653–1662
25. Martins JDP, De Carvalho ALM, Padilha AF (2012) Texture analysis of cold rolled and annealed aluminum alloy produced by twin-roll casting. Mater Res 15:97–102
26. Skrotzki W, Hünsche I, Hüttenrauch J, Oertel CG, Brokmeier HG, Höppel HW, Topic I (2008) Texture and mechanical anisotropy of ultrafine-grained aluminum alloy AA6016 produced by accumulative roll bonding. Texture Stress Microstruct 2008:1–8
27. Engler O, Hirsch J (2002) Texture control by thermomechanical processing of AA6xxx Al–Mg–Si sheet alloys for automotive applications—a review. Mater Sci Eng A 336:249–262
28. Dumoulin OGLS, Engler O (2012) Description of plastic anisotropy in AA6063-T6 using the crystal plasticity finite element method. Model Simul Mater Sci Eng 055008:1–20
29. Engler O, Vatne HE (1998) Modeling the recrystallization textures of aluminum alloys after hot deformation. JOM 50:23–27
30. ASTM E8 (2010) ASTM E8/E8M standard test methods for tension testing of metallic materials 1. Annu B ASTM Stand 4:1–27
31. Conshohocken W (1998) Standard test method for plastic strain ratio r for sheet metal 1. Methods 03:1–8
32. Bijker S, (2006) How to perform adequate optical strain measurements on a sheet metal truck bumper. Report MT06.56
33. Mishra SK, Desai SG, Pant P, Narasimhan K, Samajdar I (2009) Improved predictability of forming limit curves through microstructural inputs. Int J Mater Form 2:59–67
34. Durante M, Formisano a L a, Capece Minutolo FM (2009) The influence of tool rotation on an incremental forming process. J Mater Process Technol 209:4621–4626
35. Durante M, Formisano A, Langella A (2010) Comparison between analytical and experimental roughness values of components created by incremental forming. J Mater Process Technol 210:1934–1941

36. Durante M, Formisano A, Langella A (2011) Observations on the influence of tool-sheet contact conditions on an incremental forming process. J Mater Eng Perform 20:941–946
37. Hussain G, Gao L, Hayat N, Cui Z, Pang YC, Dar NU (2008) Tool and lubrication for negative incremental forming of a commercially pure titanium sheet. J Mater Process Technol 203:193–201
38. Chakrabarty J (2006) Theory of plasticity: third edition. Elsevier Butterworth-Heinemann, Amsterdam
39. Bramley AN, Jeswiet J, Micari F, Duflou J, Allwood J (2005) Asymmetric single point incremental forming of sheet metal. CIRP Ann Manuf Technol 54:88–114
40. Eyckens P, He S, Van Bael A, Van Houtte P, Duflou J (2007) Forming limit predictions for the serrated strain paths in single point incremental sheet forming. AIP Conf Proc 908:141. https://doi.org/10.1063/1.2740802
41. Dieter GE (2014) Mechanical metallurgy. CreateSpace Independent Publishing Platform
42. Verlinden B, Driver J, Samajdar I, Doherty RD (2014) Thermo-mechanical processing of metallic materials. Pergamon materials series. Elsevier, Amsterdam
43. Engler O, Aegerter J (2014) Texture and anisotropy in the Al–Mg alloy AA 5005—part II: correlation of texture and anisotropic properties. Mater Sci Eng A 618:663–671
44. Wen XY, Long ZD, Yin WM, Zhai T, Li Z, Das SK (2006) Texture evolution in continuous casting AA5052 aluminum alloy hot band during equi-biaxial stretching. TMS 99–107
45. Ghosh M, Miroux A, Kestens LAI (2015) Correlating r-value and through thickness texture in Al–Mg–Si alloy sheets. J Alloys Compd 619:585–591